PAPER

Modeling of Dopant Diffusion in Silicon

Scott T. Dunham[†], **Alp H. Gencer**[†], *and* **Srinivasan Chakravarthi**[†],

SUMMARY Recent years have seen great advances in our understanding and modeling of the coupled diffusion of dopants and defects in silicon during integrated circuit fabrication processes, but at the same time the ever-progressing shrinkage of device dimensions and tolerances leads to new problems and a need for even better models. In this review, we address some of the advances in the understanding of defect-mediated diffusion, focusing on the equations and parameters appropriate for modeling of dopant diffusion in submicron structures.

key words: Dopant diffusion, point defects, silicon, interstitial, vacancy, dopant/defect pairing, coupled diffusion, pair diffusion, diffusivity, equilibrium concentration, metal diffusion, lattice Monte Carlo

1. Introduction

Understanding and modeling the coupled diffusion of dopants and point defects is critical for the continuing evolution of VLSI technology. However, the development of consistent quantitative models remains a challenge due to the complexity of the interactions involved, the large number of parameters, and the difficulty in making direct measurements of critical properties. In this work, we review some of the major advances in our understanding of these processes. We start by discussing the equations describing dopant/defect diffusion and then consider the values of basic point defect and dopant diffusion parameters which enter into those equations. We then go on to consider in more detail the interactions of diffusion with extended defects as required to understand transient enhanced diffusion and dopant activation.

2. Coupled Dopant/Defect Diffusion

It has become accepted that dopants in silicon diffuse via interactions with point defects, interstitials and vacancies. The current standard model for coupled dopant/defect diffusion is the pair diffusion model [1]–[4], which assumes that dopant diffusion occurs through the formation of dopant/defect pairs that then diffuse as a unit. Thus, the effective diffusivity observed represents the diffusivity of these mobile pairs multiplied by the fraction of dopants which are paired. It is generally assumed that ionization reactions are near local equilibrium, resulting in the following diffusion/reaction equations for a system containing a single donor species (P) [5]:

$$\frac{\partial C_{\mathrm{P}^+}}{\partial t} = -R_{\mathrm{P/I}} - R_{\mathrm{P/V}} + R_{\mathrm{PI/V}} + R_{\mathrm{PV/I}} + 2R_{\mathrm{PI/PV}}, \quad (1)$$

$$\frac{\partial C_{\mathrm{I}}}{\partial t} = -\nabla \cdot J_{\mathrm{I}} - R_{\mathrm{P/I}} - R_{\mathrm{I/V}} - R_{\mathrm{PV/I}}, \quad (2)$$

$$\frac{\partial C_{\mathrm{V}}}{\partial t} = -\nabla \cdot J_{\mathrm{V}} - R_{\mathrm{P/V}} - R_{\mathrm{I/V}} - R_{\mathrm{PI/V}}, \quad (3)$$

$$\frac{\partial C_{(\mathrm{PI})}}{\partial t} = -\nabla \cdot J_{(\mathrm{PI})} + R_{\mathrm{P/I}} - R_{\mathrm{PI/V}} - R_{\mathrm{PI/PV}}, \quad (4)$$

$$\frac{\partial C_{(\mathrm{PV})}}{\partial t} = -\nabla \cdot J_{(\mathrm{PV})} + R_{\mathrm{P/V}} - R_{\mathrm{PV/I}} - R_{\mathrm{PI/PV}}. \quad (5)$$

J_{X} represents the flux of species X and $R_{\mathrm{X/Y}}$ represents the net rate per unit volume of the reaction of species X and Y (e.g., $R_{\mathrm{PV/I}}$ represents the net forward rate of reaction $\mathrm{PV} + \mathrm{I} \Leftrightarrow \mathrm{P}$). This model is commonly referred to as a "five stream model" based on the number of continuity equations for a single dopant. Each additional dopant adds three addition equations equivalent to Eqs. (1), (4) and (5), with corresponding flux and reaction terms added to the point defect equations. Both defects and pairs can exist in multiple charge states (e.g., V^-, I^{++}), but the above equations have been summed over these charge states, so that C_{I}, C_{V}, $C_{(\mathrm{PI})}$ and $C_{(\mathrm{PV})}$ represent the total concentrations of point defects or pairs. Thus, for example

$$C_{\mathrm{V}} = \sum_i C_{\mathrm{V}^i} = \sum_i \left[K_{\mathrm{V}^i} \left(\frac{n_i}{n} \right)^i C_{\mathrm{V}^0} \right], \quad (6)$$

where the superscript i represents the charge on the defect or complex, K_{X} is an equilibrium coefficient, and n and n_i are the local and intrinsic carrier concentrations. The flux and reaction terms also include sums over all the charge states, so for example:

Manuscript received December 1, 1998.
Manuscript revised

[†]The author is with the Department of Electrical and Computer Engineering at Boston University, Boston, MA, USA.
[†]The author is with the Department of Electrical and Computer Engineering at Boston University, Boston, MA, USA.
[†]The author is with the Department of Manufacturing Engineering at Boston University, Boston, MA, USA.

$$J_{(\mathrm{PV})} = -\sum_i D_{\mathrm{PV}^i}\left[\nabla C_{(\mathrm{PV})^i} + iC_{(\mathrm{PV})^i}\nabla \ln\left(\frac{n}{n_i}\right)\right]$$

$$= -\left[\sum_i D_{\mathrm{PV}^i}\left(\frac{n_i}{n}\right)^{i-1} K_{\mathrm{PV}^i}\right] \times \left[\nabla C_{(\mathrm{PV})^+} + C_{(\mathrm{PV})^+}\nabla \ln\left(\frac{n}{n_i}\right)\right] \quad (7)$$

It is necessary to determine the Fermi level in order to consider the behavior of charged species. It is possible to solve Poisson's equation in conjunction with continuity equations, but it has generally proven sufficient to simply assume local charge neutrality [6], [7] so that the electron concentration can be calculated algebraically from the dopant distribution. When other species such as clusters or extended defects are also present as discussed in Sections 4 and 5, additional continuity equations must be added and additional terms representing the formation/dissolution of these species must be included on the right hand sides of Eqs. 1–5.

Under most conditions (although not during the early stages of ion implant annealing), the dopant/defect pairing reactions (e.g., $\mathrm{P} + \mathrm{I} \Leftrightarrow \mathrm{PI}$) are fast enough to maintain the pair concentration near local equilibrium with the concentrations of isolated dopants and defects (e.g., $C_{(\mathrm{PI})^{i+1}} \cong K^i_{\mathrm{P/V}} C_{\mathrm{P}^+} C_{\mathrm{I}^i}$). Under these conditions, the five stream model can be reduced to three continuity equations (often referred to as the "fully-coupled" model) [5]:

$$\frac{\partial\left(C_{\mathrm{P}^+} + C_{(\mathrm{PI})} + C_{(\mathrm{PV})}\right)}{\partial t} = -\nabla\cdot\left(J_{(\mathrm{PI})} + J_{(\mathrm{PV})}\right) \quad (8)$$

$$\frac{\partial\left(C_{\mathrm{I}} + C_{(\mathrm{PI})}\right)}{\partial t} = -\nabla\cdot\left(J_{\mathrm{I}} + J_{(\mathrm{PI})}\right) - R \quad (9)$$

$$\frac{\partial\left(C_{\mathrm{V}} + C_{(\mathrm{PV})}\right)}{\partial t} = -\nabla\cdot\left(J_{\mathrm{V}} + J_{(\mathrm{PV})}\right) - R. \quad (10)$$

The flux terms can be rewritten as:

$$J_{(\mathrm{PV})} = -\left[\sum_i D_{\mathrm{P}}^{\mathrm{V}^i}\left(\frac{n_i}{n}\right)^i\right] \times \left[\frac{C_{\mathrm{V}^0}}{C^*_{\mathrm{V}^0}}\nabla C_{\mathrm{P}^+} + C_{\mathrm{P}^+}\nabla\left(\frac{C_{\mathrm{V}^0}}{C^*_{\mathrm{V}^0}}\right) C_{\mathrm{P}^+}\nabla \ln\left(\frac{n}{n_i}\right)\right] \quad (11)$$

where $*$ indicates equilibrium values and

$$D_{\mathrm{P}}^{\mathrm{V}^i} = D_{(\mathrm{PV})^{i+1}}\left(\frac{C_{(\mathrm{PV})^{i+1}}}{C_{\mathrm{P}^+}}\right)^* = D_{(\mathrm{PV})^{i+1}} K^i_{\mathrm{P/V}} C_{\mathrm{P}^+} C^*_{\mathrm{V}^0} \quad (12)$$

is the equilibrium intrinsic diffusivity of a dopant via vacancies of charge i. $D_{(\mathrm{PV})^{i+1}}$ is the actual pair diffusivity and $K^i_{\mathrm{P/V}}$ is an equilibrium constant. The net recombination rate can be written

$$R = k_{\mathrm{I/V}}\left(C_{\mathrm{I}} C_{\mathrm{V}} - C^*_{\mathrm{I}} C^*_{\mathrm{V}}\right), \quad (13)$$

where in general $k_{\mathrm{I/V}}$ is a function of doping and Fermi level to account for the reaction of pairs with the opposite type defect (e.g., $\mathrm{PV} + \mathrm{I} \Leftrightarrow \mathrm{P}$) as well as opposite type pairs [5].

2.1 Vacancy-Mediated Diffusion at High Doping Levels

In order to replicate the plateau regions seen in experimental results, the models of both Yoshida and Mathiot and Pfister included greatly enhanced diffusion at very high doping levels (above about $10^{20}\mathrm{cm}^{-3}$). This effect was attributed to the presence of attractive long-range dopant/vacancy interaction potentials which resulted in the interaction of vacancies with more than one dopant atom, thus increasing the number and/or effective diffusivity of pairs. A long-range interaction is a requirement for diffusion of dopant/vacancy pairs since, as noted by Hu [8], a dopant/vacancy pair in the silicon lattice must dissociate to at least third-nearest neighbor (3NN) distance to diffuse. Yoshida assumed that dopant atoms were uniformly distributed and calculated that overlapping potentials would lead to a reduction in vacancy (and thus pair) formation energy proportional to ${C_{\mathrm{P}^+}}^2$, while Mathiot and Pfister [9], [10] used an analogy to percolation to say that both the vacancy and pair fluxes increase by a factor of $F = \exp(E_B^{2NN}/kT)$ (E_B^{2NN} is the dopant/vacancy second-nearest neighbor binding energy) within a percolation cluster, with the probability of being within that percolation cluster being given by:

$$P = \begin{cases} 0, & {C_{\mathrm{P}}}^{\mathrm{T}} \leqq C^* \\ \min\left[1, K\left(\dfrac{{C_{\mathrm{P}}}^{\mathrm{T}}}{C^*} - 1\right)^{\beta}\right], & {C_{\mathrm{P}}}^{\mathrm{T}} > C^* \end{cases} \quad (14)$$

Isoconcentration experiments by Larsen *et al.* [11] have confirmed that greatly enhanced diffusion of As, Sb, Sn and Ge is observed in the presence of high phosphorus doping levels.

The models proposed by Yoshida and Mathiot and Pfister give very different predictions of how diffusivity increases with doping level. In order to gain a greater understanding of vacancy-mediated diffusion, Dunham and Wu [12]–[14] used a series of lattice Monte-Carlo (LMC) simulations. These simulations consider the biased random walk of vacancies on a doped silicon lattice, with hopping rates controlled by changes in energy associated with the dopant/vacancy interaction potential versus distance.

The result of the LMC simulations is that dopant diffusivity via dopant/vacancy pairs is enhanced by a factor $[1 + (C_D/C^*)^m]$ at high doping levels, with m ~3–4 (Fig. 1). This change leads to a rapid rise in diffusivity for donor concentrations above about $2 \times 10^{20}\mathrm{cm}^{-3}$ as observed experimentally [11]. Figure 1

also shows a match of this model to experimental data,

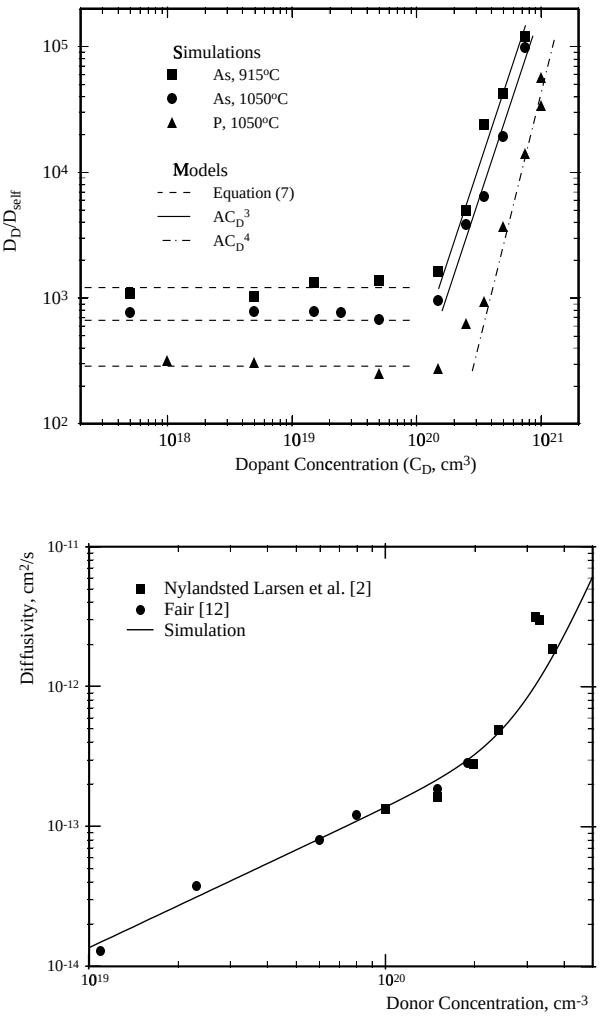

Fig. 1 *Results of lattice Monte Carlo simulations of donor diffusivity as function of doping level. Normalized diffusivity versus doping density using experimental pair binding energy for arsenic and phosphorus [15] is shown in (a). At high concentrations, the normalized diffusivity is approximately proportional to $C_D{}^m$ with $3 < m < 4$ as indicated. Also shown for comparison is the analytic predictions for diffusivity in moderately doped material [12]. These results are compared to experimental measurements [11], [18] of arsenic diffusivity at versus doping level in (b) ($T = 1050°\mathrm{C}$). The diffusivity for moderate doping levels is fit assuming diffusion via negatively-charged vacancies and then extrapolated to higher doping levels using the simulation results shown in (a).*

with the values for the parameters C^* and m taken from the results of LMC simulations [13]. Also shown for comparison are predictions of the model of Mathiot and Pfister. Note that the results are very different than predicted by a percolation model, which shows an abrupt increase in diffusivity not seen in either the LMC simulation or the data. The behavior is polynomial as predicted by Yoshida, but considering random rather than regularly-spaced dopant atoms leads to the effect occuring at lower doping levels and/or with weaker dopant/vacancy interaction potentials. The excellent agreement shown in Fig. 1 was obtained using experimental binding energies for arsenic (1.23 eV) or phosphorus (1.04 eV) from Hirata *et al.* [15], which also agree well with more recent *ab-initio* calculations [16], [17].

2.2 Consistent modeling of differences in diffusion behavior

Both Yoshida and Mathiot and Pfister assumed that phosphorus diffused primarily versus vacancies. This led to contradictions with other experimental results which indicated that phosphorus diffused primarily via interstitials (e.g., enhanced and retarded diffusion during oxidation and nitridation [19], [20]) and that enhanced diffusion in the tail region was due to an interstitial rather than a vacancy supersaturation (e.g., retarded diffusion of buried antimony layers [21], [22] and the growth of stacking faults due to P diffusion [23], [24]). More recent work has shown that it is possible to consistently model phosphorus diffusion behavior by considering a dual diffusion model, with diffusion under intrinsic conditions dominated by interstitials as needed to match OED/NRD results, but with vacancy diffusion mechanisms becoming more important at high doping levels due to the increased importance of negatively charged vacancies and the interaction of vacancies with multiple dopants [5], [25], [26]. Figure 2 shows example comparisons between such a coupled diffusion model and experimental data [5].

It is interesting to note that once the issues regarding the unusual behavior of phosphorus are resolved, that the behavior of the other dopants follows directly [25]. Boron diffusion shows similar (but slightly smaller) tail enhancements relative to phosphorus, but no plateau or kink (Fig. 3). These differences follow directly from the lower solubility compared to phosphorus and the assymmetry in the locations relative to the band-gap of negative versus positive states for vacancies and interstitials [28]. Arsenic and antimony show very little effect due to coupled diffusion as their slower diffusivity injects fewer pairs into the bulk [25].

3. Point Defect Properties

The properties of point defects clearly play a central role in controlling diffusion processes, as well as their interactions with other processes such as film growth, ion implantation and extended defect kinetics. Because the diffusion of metal atoms (as well as dopants) depends quite directly on total point defect fluxes, values for the $D_\mathrm{I}C_\mathrm{I}^*$ and $D_\mathrm{V}C_\mathrm{V}^*$ products have become broadly accepted [30]–[37]. However, there continue to exist substantial disagreements over the magnitude of

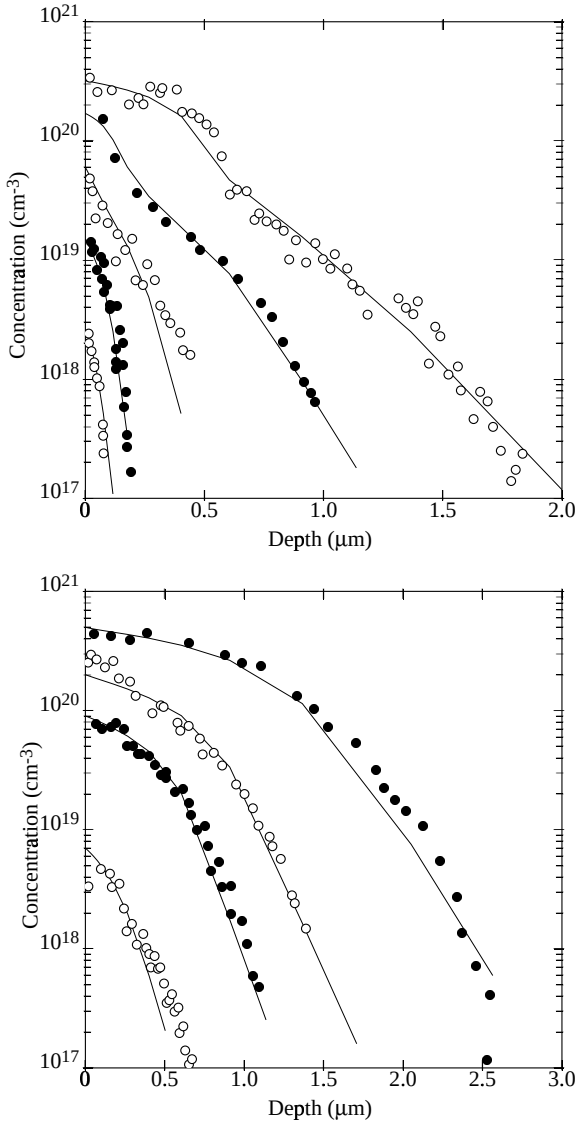

Fig. 2 Phosphorus diffusion profiles for 4 h at 900°C and 30 min at 1100°C from Yoshida [1] and Matsumoto *et al.* [27] and comparison to simulation results.

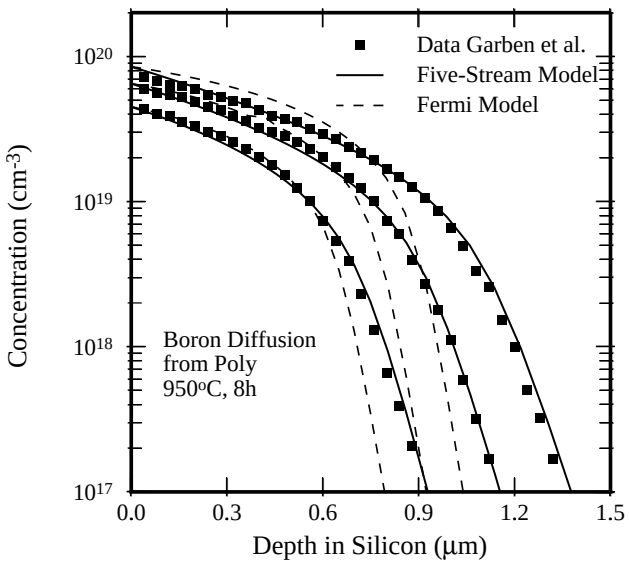

Fig. 3 Boron diffusion from implanted polysilicon from Garben *et al.* [29] and comparison to prediction of coupled diffusion model. Note that for the heaviest doping, tail diffusion is enhanced by a factor of about 4.

the diffusivities and equilibrium concentrations which go to make up these concentrations.

3.1 Interstitial parameters

The greatest attention has been focused on the diffusivity of interstitials [33], [38], with published values spanning orders of magnitude at any given temperature. However, despite the huge discrepancies in calculated parameter values, similar experiments generally give consistent and repeatable values for the effective silicon interstitial diffusivity. Specifically, experiments which measure enhanced diffusion or stacking fault growth at the wafer frontside during backside oxidation [39]–[43] or the lateral extent of oxidation enhanced diffusion (OED) [44]–[48], generally yield slow effective diffusivity values ($\approx 10^{-9}$ cm^2/sec at 1100°C). Intermediate effective diffusivity values ($> 10^{-8}$ cm^2/sec at 1100°C) have been calculated from OED of buried layers [49], [50], while metal diffusion experiments [34], [35], [51]–[54] give a higher effective diffusivity ($\approx 10^{-6}$ cm^2/sec at 1100°C). Finally, *ab-initio* [55]–[57] and tight-binding [58] calculations give similar or even higher estimates.

The repeatability of experimental measurements suggests that the analyses of the experiments rather than the experiments themselves are the source the discrepancies in calculated interstitial diffusivity values. Models used in calculating interstitial diffusivity typically over-simplify the system, using an effective diffusivity ($D_{\mathrm{I}}^{\mathrm{eff}}$) to account for all bulk interactions and a constant effective regrowth velocity ($\sigma_{\mathrm{I}}^{\mathrm{eff}}$) to account for all interface effects:

$$\frac{\partial C_{\mathrm{I}}}{\partial t} = \nabla \cdot D_{\mathrm{I}}^{\mathrm{eff}} \nabla C_{\mathrm{I}}, \tag{15}$$

$$\hat{n} \cdot D_{\mathrm{I}}^{\mathrm{eff}} \nabla C_{\mathrm{I}} = \sigma_{\mathrm{I}}^{\mathrm{eff}} (C_{\mathrm{I}} - C_{\mathrm{I}}^{*}), \tag{16}$$

where C_{I} is the interstitial concentration in silicon and $\hat{n}$ is the interface normal. However, under many conditions, additional bulk and interface interactions can be expected to play an important role.

Griffin *et al.* [38] explained these differences by assuming that trap species present in Czochralski and float-zone silicon, but absent from epitaxial silicon, slow down the propagating diffusion front of interstitials,

thus resulting in a reduced effective diffusion coefficient. The fast diffusion noted in the metal diffusion experiment is explained by assuming that the gettering or metal indiffusion process causes a much higher supersaturation of interstitials which rapidly fill the traps and allow unimpeded diffusion. Recent work has focused on carbon as the trapping species, backed up by observations of greatly reduced effective interstitial diffusivity in the presence of elevated carbon doping [59]. However, significant effects occur only when carbon concentrations exceed about 10^{17}cm^{-3} [59], while typical concentrations in both Czochralski and float-zone material are less than 10^{16}cm^{-3} [60].

The observation that low diffusivity values are calculated only when the interstitial concentration is monitored near an interface (e.g., lateral OED or backside OED experiments), while experiments which monitor defect concentrations in the bulk (e.g., buried layer or metal diffusion experiments) result in much higher diffusivity values, suggests that a more complete model for interactions with films and interfaces may be needed.

Additional information regarding the effective interface regrowth velocity for interstitials has come from analysis of reverse short channel effects (RSCE) due to transient enhanced diffusion (TED). Rafferty *et al.* [61], [62] were able to model experimentally-observed threshold voltage and body coefficient changes with channel length, but required an effective interface recombination velocity orders of magnitude larger than values which would be consistent with longer time and/or higher temperature experiments [39], [44]. Crowder *et al.* [63] came to a similar conclusion using measurements of asymmetric boron diffusion profiles in SOI structures. For both of these experiments, very small thermal budgets compared to those used in backside or lateral OED experiments were used, suggesting that the effective interface regrowth velocity starts off large, but decreases with time.

In order to account for the range of experimental observations, Dunham and Agarwal [64], [65] proposed that in addition to relatively slow interface regrowth, excess silicon (interstitials) segregate strongly to oxide films from the silicon and diffuse slowly within the film. This model represents an extension of models for OED which require that most of the interstitials generated at the interface must go into the oxide [64], [66], [67]. Verification of the model comes from observations by Celler and Trimble [68] of complete dissolution of a thin silicon layer in an SiO_2 film. The segregation process acts in many ways like an effective regrowth velocity which decreases with time. When there is a supersaturation of interstitials in the substrate, interstitials near the interface segregate to the oxide setting up a diffusion gradient within the SiO_2. Initially this results in a large flux of silicon into the oxide as the concentration gradient in the oxide is very large. As time goes on, the region of the oxide near the interface starts to "fill up" with excess silicon, reducing the concentration gradient and thus the flux into the oxide. This behavior can be confused with a slow interstitial diffusivity because of the resulting delay in the rise of interstitial supersaturation near an Si/SiO_2 interface.

Using the fast interstitial diffusivity values (and associated equilibrium concentration) determined by Bracht *et al.* [34] from metal diffusion, the model is able to accurately account for the much slower effective interstitial diffusion seen in backside OED and 2D OED experiments [65]. An example is shown in Fig. 4. In addition, the model also correctly predicts [69] the large effective regrowth velocity seen for low thermal budgets by Rafferty *et al.* [61], [62] (TED) and Crowder *et al.* [63] (OED).

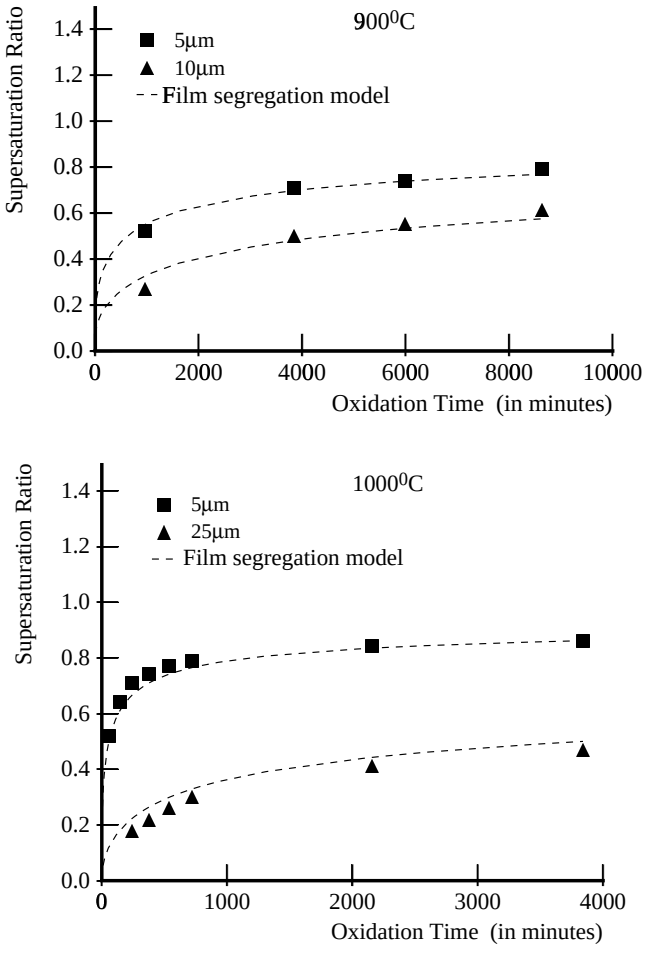

Fig. 4 *Comparison of simulation and data for time-averaged interstitial supersaturation at the center of nonoxidizing stripes. The values are normalized to the time-averaged excess supersaturation under wide oxidizing regions where maximum OED occurs. The results for the stripe widths indicated are plotted versus oxidation time at (a) 900 and (b) 1000°C. Data from Griffin [45].*

3.2 Vacancy parameters

Recently, attention has also been paid to the behavior of vacancies, for which the accepted view within the TCAD commmunity had been that they are relatively slow diffusers compared to interstitials, but are present in much larger numbers. This conclusion has been largely based on analysis of metal diffusion experiments [34],[35],[70]. In contrast, *ab-initio* [56],[57] and tight-binding MD calculations [58] find that formation energies for vacancies are on the same order or larger than that of interstitials and that the migration energy for vacancies is smaller than that of interstitials. Upon reexamining the analyses of metal diffusion experiments which gave large equilibrium concentrations and low diffusivities for vacancies, it can be observed that in order to simplify the analysis, the original work generally neglected bulk recombination and made a number of assumptions about the dominant mechanisms controlling behavior at different temperatures and time scales. Reanalyzing the most extensive data set, that of Bracht *et al.* for zinc in-diffusion [34], using a complete set of equations for coupled diffusion of metal with both interstitials and vacancies gave $C_{\mathrm{V}}^{*} \sim C_{\mathrm{I}}^{*}$ (Fig. 5) [71], four orders of magnitude smaller than originally calculated and much closer to the results of atomistic calculations. Further analysis leads to the conclusion that the $D_{\mathrm{I}}C_{\mathrm{I}}^{*}$ product is well characterized by the data and that it is possible to establish solid upper limits for $D_{\mathrm{V}}C_{\mathrm{V}}^{*}$ and C_{I}^{*}, but that C_{V}^{*} is not accurately determined by these experiments and only a relatively loose upper bound could be obtained. Platinum diffusion experiments, which previously claimed to provide direct measurement of high values of C_{V}^{*} [36], were also fit using the same parameters by considering the aggregation of carbon with interstitials into small clusters [59], with carbon concentrations consistent with densities found in device-quality Czochralski and floatzone material (10^{15}–$10^{16}\mathrm{cm}^{-3}$).

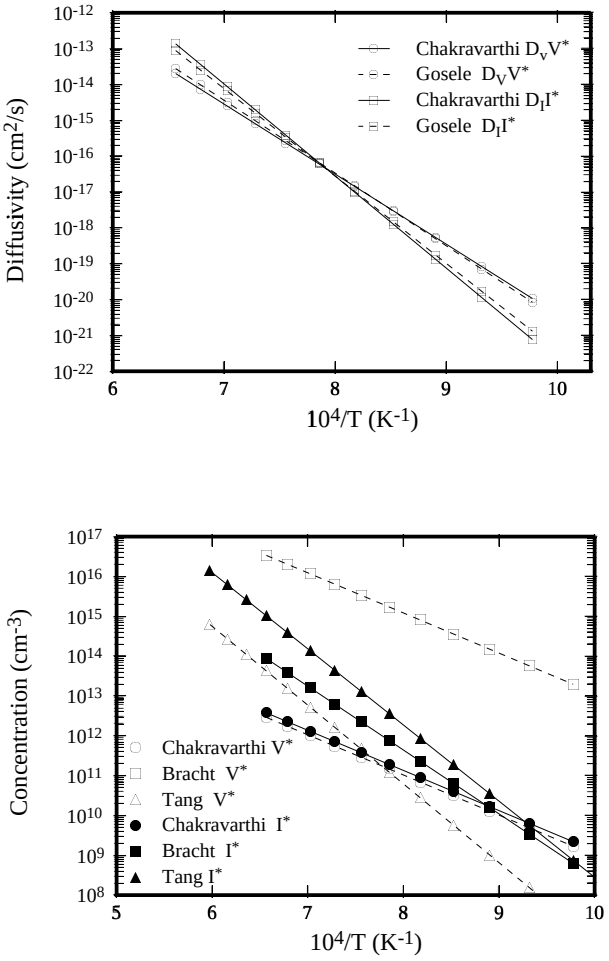

Fig. 5 Extracted values [71] of (a) $D_{\mathrm{V}}C_{\mathrm{V}}^{*}/C_s$, $D_{\mathrm{I}}C_{\mathrm{I}}^{*}/C_s$ (C_s is the silicon lattice density) and (b) C_{V}^{*} and C_{I}^{*} from fitting Zn diffusion data of Bracht *et al.* [34] and comparison to previous analyses based on both metal diffusion [34], [37] and atomistic calculations [58].

4. Transient Enhanced Diffusion

As thermal budgets have shrunk with device dimensions, the enhanced diffusion occuring during implant annealing has come to be the dominant diffusion process. This transient enhanced diffusion (TED) can be attributed to the excess point defects generated by the implanted ions and associated cascade. The density of generated point defects is generally several orders of magnitude larger than that of the implanted ions, but the numbers of interstitials and vacancies are nearly equal. Thus, under typical implant conditions, the Frenkel pairs quickly recombine leaving a much smaller net defect distribution with a total net interstitial dose approximately equal to the implanted dose (the number of extra atoms provided by the implant). Due to momentum transfer the interstitials are located slightly deeper than the vacancies leaving a surface region with a net vacancy excess and a deeper interstitial-rich region. Since the total net dose and approximate depth are close to that of the implanted ions, the initial damage is often effectively approximated by a "+1" interstitial profile corresponding to the implant [72]. This approximation is particularly effective for lighter ions such as boron for which the displacement of secondary defects is smallest.

While the "+1" model is effective at moderate doses, there are significant deviations at both higher and lower doses. For high doses, the damage is sufficient to form a continuous amorphous layer. Amorphization has been observed to occur when the density of point defects exceeds about 10% of the lattice density, upon which a transformation to the amorphous phase occurs [74]. After annealing at moderate tem-

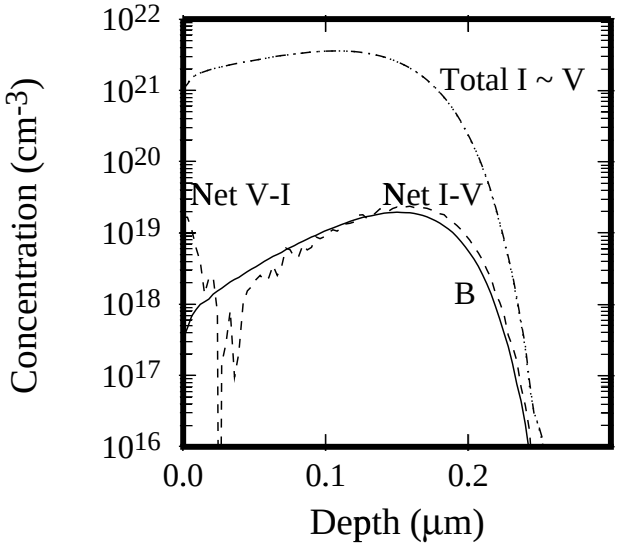

Fig. 6 Monte Carlo simulation [73] showing intial distributions of boron, interstitials and vacancies following a 40 keV, 2×10^{14} cm^{-2} B implant.

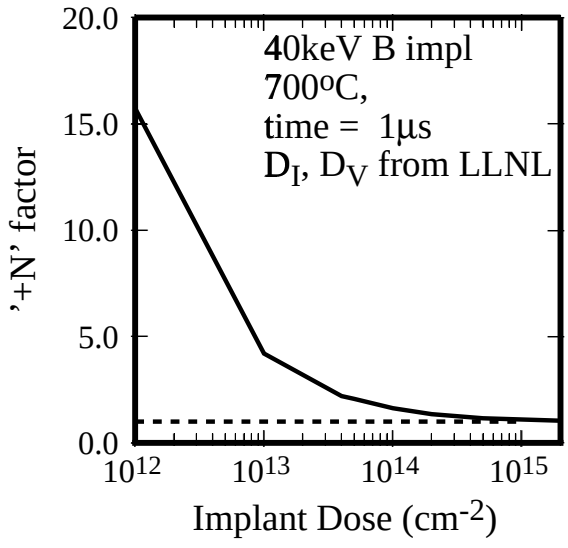

Fig. 7 Normalized net interstitial dose remaining after the initial recombination process is complete. The simulations started with the total initial defect distributions for a 40 keV B implant from a Monte-Carlo ion implant simulation (TRIM [73]).

peratures (~500°C or higher), the amorphous region regrows leaving what appears to be a nearly defect-free region. Thus, the remaining damage is limited to what is below the amorphous-crystalline interface. Higher implant doses lead to deeper amorphization and the net excess interstitial concentration following regrowth levels off or drops rather than continuing to increase.

At low doses, the assumption that Frenkel pair recombination is very fast compared to other processes breaks down as the faster diffusing defect species has a significant chance of reaching the surface before encountering the opposite type defect. Since, as discussed in Section 3, current evidence suggests that vacancies diffuse more rapidly than interstitials, this leads to an interstitial dose remaining in the silicon after nearly all vacancies have been annihilated that can be much larger than that predicted by the "+1" model. It is possible to estimate the remaining interstitial dose by modeling diffusion and recombination in the early stages of implant annealing. The results of such simulations are shown in Fig. 7 in terms of the integrated interstitial dose remaining divided by the implant dose to give an effective "+N" factor by which to scale the initial damage. When both amorphization and fast vacancy diffusion are taken into account, it is possible to accurately model the dose dependence of TED as shown in Fig. 8.

A critical observation regarding TED is that while the final junction motion depends strongly on dose and energy, the initial diffusivity enhancement is nearly independent of these factors [75], [76] (Fig. 9). These observations lead to the conclusion that excess interstitials

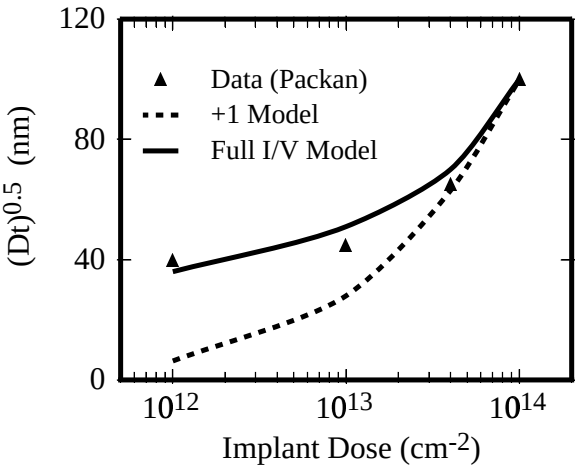

Fig. 8 Dose dependence of TED measured for boron marker layers following 200 keV Si implants from Packan [75] compared to model simulations which use a +1 or +N initial net interstitial distribution, with the value of N calculated as in Fig. 7.

aggregate into extended defects, reducing the initial supersaturation, but prolonging the TED period as the interstitials are subsequently released. This conclusion gathers strong support from the identification of these aggregates as planar {311} defects elongated in {011} directions. The number of interstitials contained within these {311} defects after short annealing matches the

implant dose, and the time period for their dissolution coincides with that of enhanced diffusion [77], [82].

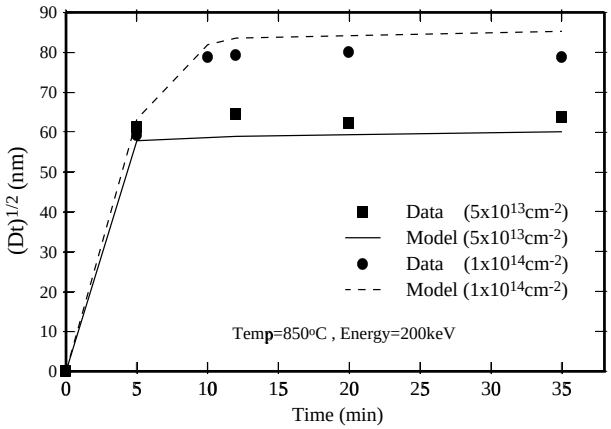

Fig. 9 Time dependence of TED. Total broadening of a deep B marker profile due to 200keV implantation of 5×10^{13} and 10^{14}cm^{-2} ^{29}Si at 200 keV with annealing at 850°C. Data from Packan [75] and comparison to model prediction.

As seen in Fig 10, TED depends strongly on the depth of the implant as controlled by the implant energy. As with changes in dose, the original enhancements are nearly unchanged, but the time period over which TED lasts is modified. The scaling of TED with energy implies that the surface is the primary sink for interstitials. This has been confirmed through etch-back experiments which conclude that the effective surface recombination length ($D_{\rm I}/\sigma_{\rm I}$) is less than 100 nm [78]. Based on the experimental observations discussed above, it is possible to come up with a simple model for the estimation of TED effects. If the formation of {311} defects is associated with an effective interstitial solubility $C_{\rm I}^{311}$ which is maintained through the growth/dissolution of these defects, then the flux of interstitials to the surface can be approximated by:

$$J_{\rm I}^{\rm TED} \cong D_{\rm I} C_{\rm I}^{311}/R_p, \tag{17}$$

where R_p is the average depth of net interstitial distribution (approximately the implant range). The period over which TED lasts then is just:

$$\tau_{\rm TED} = \frac{Q_{\rm I}}{J_{\rm I}^{\rm TED}} = \frac{Q_{\rm I} R_p}{D_{\rm I} C_{\rm I}^{311}}, \tag{18}$$

where the net excess implant dose $Q_{\rm I} = NQ_{\rm implant}$ based on an "$+N$" model.

During TED, the interstitial supersaturation is $C_{\rm I}^{311}/C_{\rm I}^*$, so the amount of excess diffusion expected during TED is given by:

$$(Dt)_{\rm TED} = D_{\rm A}^* \tau_{\rm TED} f_{\rm I} \frac{C_{\rm I}^{311}}{C_{\rm I}^*} = \frac{D_{\rm A}^* f_{\rm I} Q_{\rm I} R_p}{D_{\rm I} C_{\rm I}^*}, \tag{19}$$

where $D_{\rm A}^*$ is the dopant diffusivity under equilibrium conditions. Note that the activation energy of dopant diffusion is less than that of self-diffusion via interstitials ($D_{\rm I} C_{\rm I}^*$), so that diffusion due to TED is actually increased as the annealing temperature is reduced (as long as sufficient time is allowed for completion of TED). It is also notable that TED depends primarily on the $D_{\rm I} C_{\rm I}^*$ product rather than the terms independently as discussed in Section 3.

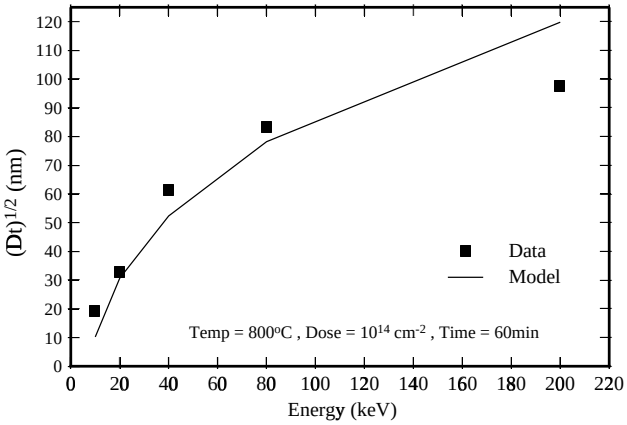

Fig. 10 Energy dependence of TED. Total broadening of a deep B marker profile due to implantation of 10^{14}cm^{-2} ^{29}Si with annealing at 800°C for 60 min. Data from Packan [75] and comparison to model prediction.

Although this simple model (which we will refer to as a one-moment model as it keeps track only of the total number of clustered interstitials) provides good estimates for the final amount of TED, it does not accurately capture the time evolution of the enhanced diffusion or the dissolution of {311} defects. If {311} defects establish a constant effective solubility as the simple model implies, then their dissolution would be approximately linear (modified by any shift of the effective depth over time). In contrast, as shown in Fig. 11 [82], the dissolution is approximately an exponential decay. Similarly, TED is not actually uniform during the TED period. Instead it drops significantly over the course of the TED period (Fig 12).

Both {311} and TED evolution can be modeled by considering a range of {311} defect sizes associated with ripening of the population during annealing, leading in turn to a reduction in the effective solubility. The aggregation process is driven by the change in system free energy. The defect energy depends strongly on size and can be written as the sum of a volume term which represents the change in energy upon adding a solute atom to an arbitrarily large defect, plus the excess energy associated with finite size, including contributions from interface and strain energies:

$$\Delta G_n = -nkT \ln\left(\frac{C_{\rm I}}{C_{\rm I}^{311}}\right) + \Delta G_n^{\rm exc}, \tag{20}$$

where n is the number of solute atoms, and $C_{\rm I}^{311}$ is the solid solubility. The form of $\Delta G_n^{\rm exc}$ depends on the

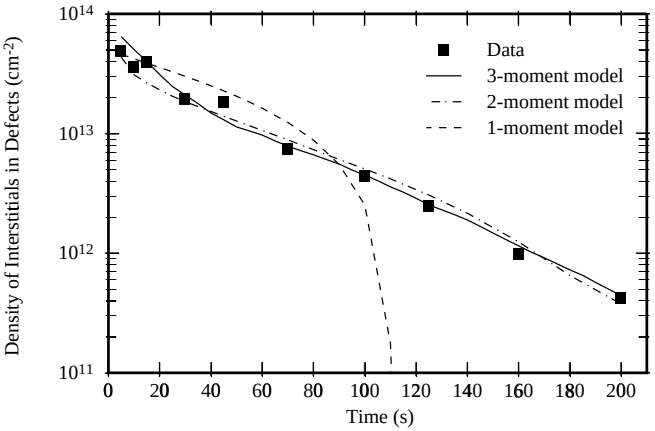

Fig. 11 Comparison of 1, 2 and 3-moment models for evolution of {311} defects. Both 2 and 3-moment models capture the exponential decay of interstitials in {311} defects. However, since the 1-moment model doesn't take the ripening process into account, it predicts an almost linear decay in m_1. Data from Eaglesham *et al.*[82]

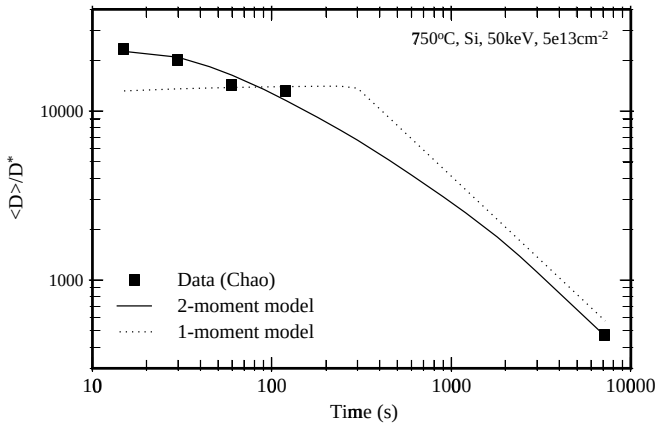

Fig. 12 Comparison of 1 and 2-moment models for short time diffusivity enhancements. Data from Chao[84] for a $5 \times 10^{13}\,\mathrm{cm}^{-2}$ 50 keV implant with anneals at 750°C.

defect structure and is chosen to match experimental results under the constraint that it varies sublinearly with size, so that C_{I}^{311} remains the asymptotic solubility [79].

It is possible to consider the full {311} size distribution ($f_n(x,t)$, the density per unit volume of defects of size n at a given location and time), which evolves through the addition or emission of interstitials:

$$\frac{df_n}{dt} = I_{n-1} - I_n, \tag{21}$$

where I_n is the net rate (per unit volume) at which interstitials are added to size n defects to form size $n+1$ defects. Since each growth step from n to $n+1$ involves a solute atom, a term must be subtracted from the interstitial continuity equation of the form:

$$R_{\mathrm{I}}^{311} = 2I_1 + \sum_{2}^{\infty} I_n, \tag{22}$$

where the factor of 2 for the I_1 is due to the fact that two solute atoms are required to make a cluster of size 2. The net rate at which precipitates in the population grow from size n to $n+1$ is [79]–[81]

$$I_n = \frac{DA_n(C_{\mathrm{I}} f_n - C_n^* f_{n+1})}{R_n + \lambda} \tag{23}$$

where A_n is the surface area of a precipitate with n solute atoms, R_n is its radius, $\lambda = D/k_n$, and k_n is the interface reaction rate. C_n^* is the concentration of solute atoms for which there is no change in the system energy for a precipitate growing from size n to $n+1$ ($g_n = d_{n+1}$):

$$\begin{aligned} C_n^* &= C \exp\left(\frac{\Delta G_{n+1} - \Delta G_n}{kT}\right) \\ &= C_{\mathrm{I}}^{311} \exp\left(\frac{\Delta G_{n+1}^{\mathrm{exc}} - \Delta G_n^{\mathrm{exc}}}{kT}\right) \end{aligned} \tag{24}$$

Modeling the full extended defect distribution is effective, but having to solve a large set of extra differential equations for each defect size at each spatial node adds a huge computational burden. A much more efficient approach is to consider the evolution of some subset of the moments of the size distribution. Evolution equations can be derived by assuming a form for the size distribution given the moments ($m_i = \sum_2^\infty n^i f_n$). The most general approach is to consider the distribution that minimizes the free energy given the moments [79]. Alternatively, it has been observed that {311} defects have an approximately log-normal size distribution ($f_n = z_0 \exp\left[-ln(n/z_1)^2/z2\right]$) with a fixed value of $z_2 = 0.8$ [85]. Figure 11 includes a comparison to both a simple linear decay as well as the moment-based approach using either three moments (m_0, m_1 and m_2) and an energy minimizing closure assumption or two moments (m_0 and m_1) and a log-normal distribution. These models are also used to compare to data for the time evolution of TED (Fig. 12). Both of the moment-based models do a good job of matching {311} defect kinetics and more importantly accurately predict TED kinetics.

At high doses, in addition to {311} defects, dislocation loops also form. In contrast to {311} defects, dislocation loops are very stable and can withstand relatively long thermal cycles. Thus, the interstitials which aggregate to form loops generally do not contribute to diffusion for thermal cycles typical of submicron devices. The nucleation and growth of dislocation loops can also be modeled using moment-based techniques. Experimental observations indicate that loops nucleate via the unfaulting of {311} defects [86]. Assuming that for smaller sizes it is energetically more favorable to stay as a {311} defect, but above a certain size (around $n = 2000$) it is more favorable to transform into a dislocation loop. The transfer rate from {311} defects into

dislocation loops as a function of defect size can be expressed as:

$$R_n^{\rm loop} = \frac{D_{\rm I}}{b^2}\left[f_n^{\{311\}} - f_n^{\rm loop}\exp\left(-\frac{\Delta G_n^{\{311\}} - \Delta G_n^{\rm loop}}{kT}\right)\right] \quad (25)$$

where b is a "capture distance." A value of about 20 μm for b matches experimental results, indicating that the transfer from {311} defects into dislocation loops is a rather slow process.

In conjunction with model and parameters for {311} defects described above, this approach is able to correctly model the transformation of {311} defects into dislocation loops, as well as the correct Ostwald ripening behavior (Fig. 13). Similar matches were obtained for data by Lui *et al.*, [88] that included longer anneals which led to substantial loop dissolution. The relatively slow dissolution rate of dislocation loops stems from the facts that they can grow very large and $C_{\rm ss}$ for loops is approximately $C_{\rm I}^*$. This results in C_n^* for loops being close to $C_{\rm I}^*$, so that they sustain only a small super-saturation of interstitials. Since these loops are deep in the substrate and sustain only a minimal supersaturation, the flux to the surface is small and thus they dissolve slowly.

5. Dopant Activation

Another critical process controlling dopant redistribution is the formation of dopant clusters or precipitates which both immobilize the dopants as well as reduce or eliminate their electrical activity. Due to volume differences, it is common for these clusters to incorporate point defects along with dopants (e.g., B/I and As/V). The most general approach considers arbitrary cluster compositions which evolve in a multi-dimensional size space (e.g., $f_{n,m}(x,t)$ to represent the concentration of B_nI_m clusters). For such a system, direct solution of the full set of discrete rate equations becomes even more computationally expensive. However, it is possible to extend the moment-based approach to this system. The free energy for a B_nI_m cluster becomes a function of both boron and interstitial concentrations, as well as size [79]:

$$\Delta G_{n,m} = -nkT\ln\left(\frac{C_B}{C_B^{ss}}\right) - mkT\ln\left(\frac{C_I}{C_I^{ss}}\right) + \Delta G_{n,m}^{\rm exc} + \Delta G_{n,m}^{\rm stress}, \quad (26)$$

The stress energy can be estimated from elasticity theory to be of the form [79]:

$$\Delta G_{n,m}^{\rm stress} = H_n + \frac{\alpha}{n}(m - \gamma n)^2. \quad (27)$$

If there were no point defect supersaturation, the optimum number of incorporated interstitials would be $m^* = \gamma n$. However, when $C_{\rm I} > C_{\rm I}^*$, the optimum number of point defects incorporated can be found by minimizing the free energy to be:

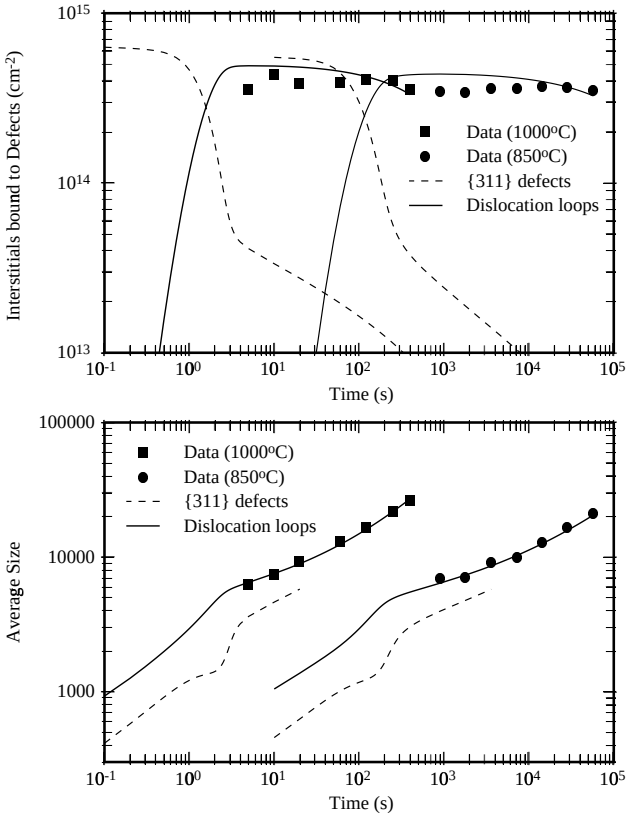

Fig. 13 Evolution of density of (a) interstitials in extended defects (m_1) and (b) average defect size (m_1/m_0) with comparison to model. Data from Pan *et al.*[87] for 1×10^{16} cm^{-2} Si implant at 50 keV with anneals at 1000° C and 850° C.

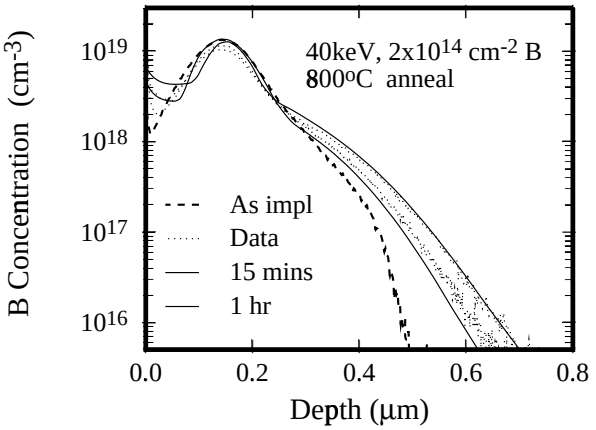

Fig. 14 *Simulations results for a $2 \times 10^{14}\text{cm}^{-2}$, 40 keV B implant annealed at 800°C with KPM model. Also shown for comparison are SIMS data from Intel [91].*

$$m^* = n\left(\gamma + \frac{kT}{2\alpha}\log(C_\text{I}/C_\text{I}^*)\right), \tag{28}$$

which leads to an effective solid solubility of:

$$C_\text{ss}^\text{eff} = C_\text{ss}\left(\frac{C_\text{I}}{C_\text{I}^*}\right)^{-\gamma}\exp\left[-\frac{kT}{4\alpha}\left(\log(C_\text{I}/C_\text{I}^*)\right)^2\right] \tag{29}$$

It is evident from the above equation that the effective solubility decreases with increase in interstitial supersaturation as observed experimentally. We find using this approach we can successfully fit medium dose TED data [91] as shown in Fig. 14.

Alternatively, it is possible to model the deactivation process by cluster-based models where we solve rate equations for a limited set of cluster sizes. Using a large set of cluster size ranges, both atomistic and contiuum models have been successful in simulating clustering of boron [89], [92]. Based on *ab-initio* calculations, which indicate that B_3I is the predominant cluster species, it is possible to derive a simple single cluster model that duplicates the results of these multi-cluster models [90]. The continuum model thus derived uses only a single reaction, that for B_3I, with the rate of formation given by [93]

$$R_{\text{B}_3\text{I}} = k^r_{\text{B}_3\text{I}}(K_{\text{B}_3\text{I}}\text{C}_\text{B}^3\text{C}_\text{I} - \text{C}_{\text{B}_3\text{I}}) \tag{30}$$

Figs. 15(a) and (b) show examples of comparison of the single cluster model to the full models, as well as to data from Intel [91] for TED at 800°C.

6. Conclusions

In summary, coupled pair diffusion models provide the basis for understanding dopant diffusion in silicon and can explain a broad range of experimental observations. However, important gaps in our knowledge still remain, particularly due to the large number of model parameters and the challenges associated with performing accurate experimental measurements, which make it very

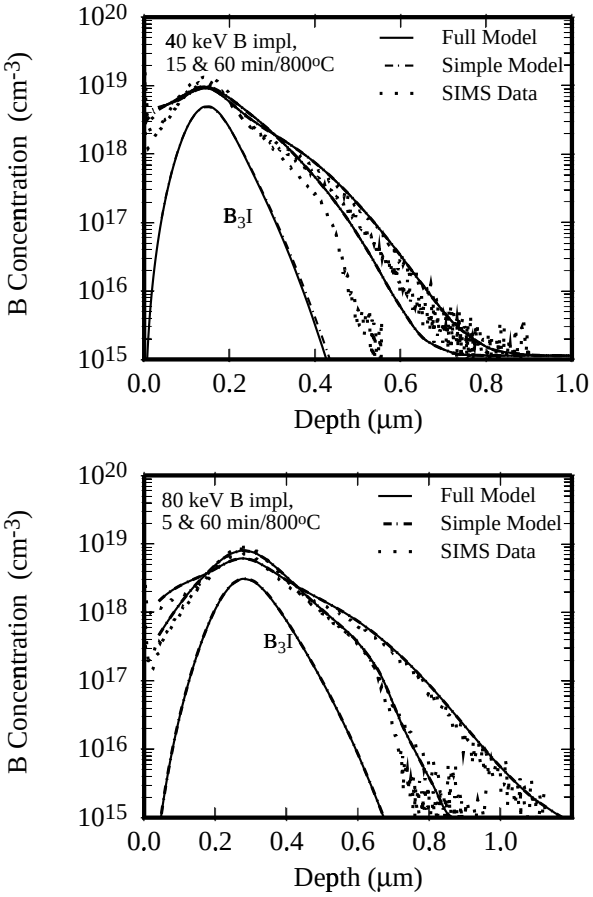

Fig. 15 *Comparison of full model with the simplified model for (a) 40keV and (b) 80keV, $2 \times 10^{14}\text{cm}^{-2}$ B implants annealed at 800°C for various times. Also shown for comparison are SIMS data from Intel [91]. Note that the full model and simple model show indistinguishable final profiles. The B_3I concentrations for the two models (shown after a 1 h anneal) are also nearly identical.*

difficult to fully characterize the system. A critical issue discussed in this review is interactions of point defect and dopant diffusion processes with extended defects, which dominates the diffusion behavior during ion implant annealing.

7. Acknowledgment

This work was supported in part by the Semiconductor Research Corporation and the National Science Foundation.

References

[1] M. Yoshida, *Jap. J. Appl. Phys.* **18**, 479 (1979).
[2] M. Yoshida, *Jap. J. Appl. Phys.* **22**, 1404 (1983).
[3] D. Mathiot and J. C. Pfister, *J. Appl. Phys.* **53**, 3035 (1982).
[4] D. Mathiot and J. C. Pfister, *J. Appl. Phys.* **55**, 3518 (1984).
[5] S. T. Dunham, *J. Electrochem. Soc.* **139**, 2628 (1992).
[6] S. M. Hu and S. Schmidt, *J. Appl. Phys.* **39**, 4273 (1968).
[7] P. M. Fahey, P. B. Griffin and J. D. Plummer, *Rev. Mod. Phys.* **61**, 289 (1989).
[8] S. M. Hu, *Phys. Rev.* **180**, 773 (1969).
[9] D. Mathiot and J. C. Pfister, *J. Phys. Lett.* **43**, L-453 (1982).
[10] D. Mathiot and J. C. Pfister, *J. Appl. Phys.* **66**, 1970 (1989).
[11] A. Nylandsted Larsen, K. Kyllesbech Larsen, P. E. Andersen, B. G. Svensson, *J. Appl. Phys.* **73**, 691 (1993).
[12] S. T. Dunham and C. D. Wu, **NUPAD V Proceedings**, 101 (1994).
[13] S. T. Dunham and C. D. Wu, *J. Appl. Phys.* **78**, 2362 (1995).
[14] S. T. Dunham and C. D. Wu, in **Simulation of Semiconductor Devices and Processes (SISDEP/SISPAD'95)**, H. Ryssel, ed. (Springer-Verlag, Wien, Austria, 1995) pp. 476–479.
[15] M. Hirata, M. Hirata and H. Saito, *J. Phys. Soc. Jap.* **27**, 405 (1969).
[16] J. S. Nelson, private communication.
[17] O. Pankratov, private communication.
[18] R. B. Fair in **Impurity Doping Processes in Silicon**, F. F. Y. Yang, ed. (North-Holland, New York, 1981) p. 315.
[19] P. Fahey, G. Barbuscia, M. Moslehi and R. W. Dutton, *Appl. Phys. Lett.* **43**, 683 (1983).
[20] H.-J. Gossmann, T. E. Haynes, P. A. Stolk, D. C. Jacobson, G. H. Gilmer, J. M. Poate, H. S. Luftman, T. K. Mogi and M. O. Thompson, *Appl. Phys. Lett.* **71**, 3862 (1997).
[21] R. M. Harris, D. A. Antoniadis, *Appl. Phys. Lett.* **43**, 937 (1983).
[22] P. Fahey, R. W. Dutton, S. M. Hu, *Appl. Phys. Lett.* **44**, 777 (1984).
[23] C. L. Claeys, G. L. Declerk and R. J. Van Overstraeten, in **Semiconductor Characterization Techniques**, P. A. Barnes and G. A. Rozgonyi, eds. (Electrochem. Soc., Pennington, NJ, 1978) p. 366.
[24] K. Nishi and D. A. Antoniadis, *J. Appl. Phys.* **59**, 1117 (1986).
[25] S. T. Dunham, in **1993 International Workshop on VLSI Process and Device Modeling (VPAD 1993)**, K. Asada, ed. (Japan, 1993) pp. 46-49.
[26] S. T. Dunham and F. P. Wittel, in **Process Physics and Modeling in Semiconductor Technology**, G. R. Srinivasan, C. S. Murthy and S. T. Dunham, eds. (Electrochem. Soc. Proc. Vol. **96-4**, Pennington, NJ, 1996) pp. 27-36.
[27] S. Matsumoto, M. Yoshida and T. Niimi, *Jap. J. Appl. Phys.* **13**, 1899 (1974).
[28] M. D. Giles, *IEEE Trans. CAD* **8**, 460 (1989).
[29] B. Garben, W. A. Orr-Arienzo, and R. F. Lever, *J. Electrochem. Soc.* **133**, 2152 (1986).
[30] U. Gösele and T. Y. Tan, in **Defects in Semiconductors II**, S. Mahajan and J. W. Corbett, eds., (North-Holland, New York, 1983) p. 45.
[31] F. Morehead in **Defects in Electronic Materials**, ed. by M. Stavola, S. J. Pearton and G. Davies (Mat. Soc. Proc. **104**, Pittsburgh, PA, 1987) p. 99.
[32] P. M. Fahey, P. B. Griffin and J. D. Plummer, *Rev. Mod. Phys.* **61**, 289 (1989).
[33] W. Taylor and U. Gösele, in **Process Physics and Modeling in Semiconductor Technology**, G. R. Srinivasan, K. Taniguchi and C. S. Murthy, eds. (Electrochem. Soc. Proc. Vol. **93-6**, Pennington, NJ, 1993) pp. 108-119.
[34] H. Bracht, N. A. Stolwijk, and H. Mehrer, *Phys. Rev. B* **52**, 16542 (1995).
[35] F. Morehead, in **Defects in Electronic Materials**, M. Stavola, S. J. Pearton and G. Davies, eds. (Mat. Soc. Proc. **104**, Pittsburgh, PA, 1988) p. 99-104.
[36] H. Zimmermann and H. Ryssel, *J. Electrochem. Soc.* **139**, 256 (1992).
[37] U. Gösele, A. Plöβl, and T. Y. Tan, *Electrochemical Soc. Proc.* **96-4**, 309 (1996).
[38] P. B. Griffin, S. T. Ahn, W. A. Tiller, and J. D. Plummer, *Appl. Phys. Lett.* **51**, 115 (1987).
[39] S. T. Ahn, J. D. Shott, and W. A. Tiller, in **Proceedings, Electrochemical Society Meeting**, Oct. 1986.
[40] S. T. Ahn, PhD thesis, Stanford University, Sept. 1988.
[41] E. Scheid and P. Chenevier, *Phys. Stat. Sol.* **93**, 523 (1986).
[42] K. Taniguchi and D. A. Antoniadis, *Appl. Phys. Lett.* **42**, 961 (1983).
[43] M. Budil, M. Heinrich, M. Schrems, and H. Potzl, *J. Electrochem. Soc.* **137**, 3931 (1990).
[44] P. B. Griffin and J. D. Plummer, in **Proc. Electrochem. Soc. Fall 1996 Meeting**, Oct 1986.
[45] P. B. Griffin, PhD thesis, Stanford University, December 1989.
[46] K. Taniguchi and D. A. Antoniadis, *Appl. Phys. Lett.*, **46**, 944 (1985).
[47] A. M. Lin, R. W. Dutton, and D. A. Antoniadis, *Appl. Phys. Lett.* **35**, 799 (1979).
[48] S. Mizuo and H. Higuchi, *Jap. J. Appl. Phys.* **21**, 272 (1982).
[49] P. B. Griffin, P. M. Fahey, J. D. Plummer, and R. W. Dutton, *Appl. Phys. Lett.* **47**, 319 (1985).
[50] A. M. Agarwal and S. T. Dunham, *Appl. Phys. Lett.* **63**, 800 (1993).
[51] G. B. Bronner and J. D. Plummer, in **Mat. Res. Soc. Symp. Proc. 36**, 49 (1985).
[52] T. Y. Tan and U. Gosele, *Appl. Phys. A* **37**, 1 (1985).
[53] N. A. Stolwijk, B. Schuster, and J. Holzl. *Appl. Phys. A* **33**, 133 (1984).
[54] S. Mantovani, F. Nava, C. Nobili, and G. Ottaviani, *Phys. Rev. B* **33**, 5536 (1986).
[55] Y. Bar-Yam and J. D. Joannopoulos, *Phys. Rev. Lett.* **52**, 1129 (1984)
[56] C. S. Nichols, C. G. Van de Walle and S. T. Pantelides, *Phys. Rev. B.* **40**, 5484 (1989)
[57] J. Zhu, T. Diaz de la Rubia, L. H. Yang, C. Mailhiot and G. H. Gilmer, *Phys. Rev B.* **54**, 4741 (1996); J. Zhu, personal communication.
[58] M. Tang, L. Colombo, J. Zhu and T. Diaz de la Rubia,

Phys. Rev B. **55**, 14279 (1997).
[59] H.-J. Gossmann, P.A. Stolk, D.J. Eaglesham, C.S. Rafferty, J.M. Poate, Appl. Phys. Lett. 67, 3135 (1995).
[60] P. Burggraaf, *Semi. Int.* **7**, 54 (1990).
[61] C. S. Rafferty, M. D. Giles, H.-H. Vuong, S. A. Eshraghi, M. R. Pinto and S. J. Hillenius, in **1993 International Workshop on VLSI Process and Device Modeling (VPAD 1993)**, K. Asada, ed. (Japan, 1993) pp. 148-149.
[62] C. S. Rafferty, S. A. Eshraghi, M. R. Pinto, S. J. Hillenius and H.-H. Vuong, #12.6 IEDM 1993 Proceedings.
[63] S. Crowder, P. B. Griffin and J. D. Plummer, in **Process Physics and Modeling in Semiconductor Technology**, G. R. Srinivasan, K. Taniguchi and C. S. Murthy, eds. (Electrochem. Soc. Proc. Vol. **93-6**, Pennington, NJ, 1993) pp. 108-119.
[64] S. T. Dunham, *J. Appl. Phys.* **71**, 685 (1992).
[65] A.M. Agarwal and S.T. Dunham, *J. Appl. Phys.* **78**, 5313 (1995)
[66] S. T. Dunham and J. D. Plummer, *J. Appl. Phys.* **57**, 2541 (1986).
[67] S. T. Dunham, in **Second Intl. Symp. on ULSI Science and Tech.**, C. M. Osburn and J. Andrews, eds., (Electrochem. Soc. Proc. 89-9, Pennington, NJ, 1989).
[68] G. K. Celler and L. E. Trimble, *Appl. Phys. Lett.* **54**, 1427 (1989).
[69] S.T. Dunham and A.M. Agarwal, in **ULSI Science and Technology**, E.M. Middlesworth and H.Z. Massoud, eds. (Electrochem. Soc. Proc., Pennington, NJ, 1995).
[70] H. Zimmermann and H. Ryssel, *Appl. Phys. A* **55**, 121 (1992).
[71] S. Chakravarthi and S. T. Dunham, in **Defects and Diffusion in Silicon Processing**, S. Coffa, T. de la Rubia, C. Rafferty, and P. Stolk, eds. (Mat. Res. Soc. Proc., Pittsburgh, PA, 1997).
[72] M. D. Giles, *J. Electrochem. Soc.* **138**, 1160 (1991).
[73] O. Vancauwenberghe, N. Herbots and O. Hellman, *J. Vac. Sci. Tech. B***9**, 2027 (1991).
[74] L. A. Christel, J. F. Gibbons and T. W. Sigmon, *J. Appl. Phys.* **52**, 7143 (1981).
[75] P. A. Packan, PhD thesis, Stanford University, February 1991.
[76] N. E. B. Cowern, K. T. F. Janssen and H. F. F. Jos, *J. Appl. Phys.* **68**, 6191 (1990).
[77] N. E. B. Cowern, G. F. A. van de Walle, P. C. Zalm and D. W. E. Vandenhoudt, *J. Appl. Phys.* **65**, 2981 (1994).
[78] D. R. Lim, C. S. Rafferty and F. P. Klemens, *Appl. Phys. Lett.* **67**, 2302 (1995).
[79] Scott T. Dunham, Iuval Clejan and Alp H. Gencer, *Mat. Sci. Eng. A***238**, 152 (1997).
[80] S.T. Dunham, *J. Electrochem. Soc.* **142**, 2823 (1995).
[81] S.T. Dunham, in **Silicon Materials Science & Technology**, H. Huff, W. Bergholz, and K. Sumino, eds.(Electrochem. Soc. Proc., Pennington, NJ 1994) p 711.
[82] D.J. Eaglesham, P.A. Stolk, H.J. Gossmann and J.M. Poate, *Appl. Phys. Lett.* **65**, 2305 (1994).
[83] A.H. Gencer and S.T. Dunham, *J. Appl. Phys.* **81**, 631 (1997).
[84] H.S. Chao, PhD thesis, Stanford University, July 1997.
[85] G.Z. Pan and K.N. Tu, *J. Appl. Phys.* **82**, 601 (1997).
[86] D.J. Eaglesham, P.A. Stolk, H.J. Gossmann, T.E. Haynes, and J.M. Poate, *Nuc. Inst. and Meth. B* **106**, 191 (1995).
[87] G.Z. Pan, K.N. Tu and S. Prussin, *Appl. Phys. Lett.* **68**, 1654 (1996).
[88] J. Lui, M.E. Law and K.S. Jones, *Solid State Electron.* **38**, 1305 (1995).
[89] A.D. Lilak, S.K. Earles, K.S. Jones, M.E. Law, and M.D. Giles, in IEDM Technical Digest, IEEE, p. 493, 1997.
[90] J. Zhu, M. J. Caturla, M. Johnson, and T.D. de la Rubia, private communication.
[91] M.D. Giles *et al.*, TED SIMS data from Intel Corporation.
[92] M. J. Caturla, M. D. Johnson and T. Diaz de la Rubia, **72** 2736 (1998).
[93] S. Chakravarthi and S. T. Dunham, in **Simulation of Semiconductor Processes and Devices (SISPAD'98)**.